catalysts

MDPI

Article

Methane Activation and Coupling Pathways on Ni_2P Catalyst

Abdulrahman Almithn *, Salem N. Alghanim, Abdullah A. Mohammed, Abdullah K. Alghawinim, Mazen A. Alomaireen, Zaid Alhulaybi and SK Safdar Hossain

Department of Chemical Engineering, College of Engineering, King Faisal University, Al Ahsa 31982, Saudi Arabia
* Correspondence: aalmithn@kfu.edu.sa

Abstract: The direct catalytic conversion of methane (CH_4) to higher hydrocarbons has attracted considerable attention in recent years because of the increasing supply of natural gas. Efficient and selective catalytic conversion of methane to value-added products, however, remains a major challenge. Recent studies have shown that the incorporation of phosphorus atoms in transition metals improves their selectivity and resistance to coke formation for many catalytic reactions. In this work, we report a density function theory-based investigation of methane activation and C_2 product formation on $Ni_2P(001)$. Our results indicate that, despite the lower reactivity of Ni_2P relative to Ni, the addition of phosphorus atoms hinders excessive dehydrogenation of methane to CH* and C* species, thus reducing carbon deposition on the surface. CH_3* and CH_2* moieties, instead, are more likely to be the most abundant surface intermediates once the initial C–H bond in methane is activated with a barrier of 246 kJ mol^{-1}. The formation of ethylene from $2CH_2$* on Ni_2P is facile with a barrier of 56 kJ mol^{-1}, which is consistent with prior experimental studies. Collectively, these findings suggest that Ni_2P may be an attractive catalyst for selective methane conversion to ethylene.

Keywords: methane activation; dehydrogenation; nickel phosphides; ethylene; density functional theory

check for updates

Citation: Almithn, A.; Alghanim, S.N.; Mohammed, A.A.; Alghawinim, A.K.; Alomaireen, M.A.; Alhulaybi, Z.; Hossain, S.S. Methane Activation and Coupling Pathways on Ni_2P Catalyst. *Catalysts* **2023**, *13*, 531. https://doi.org/10.3390/catal13030531

Academic Editors: Tamer S. Saleh, Nesreen S. Ahmed and Mohamed Mokhtar M. Mostafa

Received: 3 January 2023
Revised: 13 February 2023
Accepted: 24 February 2023
Published: 6 March 2023

1. Introduction

Recent years have seen a dramatic increase in catalytic studies focusing on the transformation of methane (CH_4) into value-added products [1–9]. Conversion of methane into high-value chemicals at low operating conditions is a critical process to utilize the increasing production of natural gas, as well as to mitigate greenhouse gas emissions. Methane is considered a major contributor to global warming along with carbon dioxide. Currently, longer alkanes and olefins are produced from methane indirectly using Fischer-Tropsch synthesis [10]. It involves the catalytic oxidation of methane to syngas (CO and H_2) followed by production of methanol and other valuable products. However, the high operating pressures and temperatures required for this process make it energy-intensive and economically costly. It is also possible to convert methane directly and efficiently into higher hydrocarbons through selective activation and coupling in a single-step process [9], but this remains a major challenge in the field of heterogenous catalysis because methane has a high C–H bond activation energy (439 kJ mol^{-1}), which requires extreme conditions to activate (temperatures > 700 °C) [11]. Moreover, once the initial C–H bond is cleaved, which is the most difficult step, subsequent C–H bond activation steps can occur rapidly due to the high temperature and cannot be controlled to selectively produce high-value chemicals. Instead, coke formation becomes prevalent, which severely impacts catalyst performance and stability.

Many different catalysts have been experimentally and theoretically investigated for oxidative and non-oxidative coupling of methane. In the oxidative coupling process, first reported by Keller and Bhasin [12], methane is converted into ethane or ethylene at temperatures higher than 700 °C according to the following equations:

$$2CH_4 + \frac{1}{2}O_2 \rightarrow C_2H_6 + H_2O \quad (1)$$

$$2CH_4 + O_2 \rightarrow C_2H_4 + 2H_2O \quad (2)$$

However, the higher reactivity of C_2 products compared to methane at the operating conditions leads to deep oxidation to carbon oxides (CO_x) and low C_2 selectivity. Low-temperature methane activation has been recently reported using the IrO_2(110) surface which activates methane at 150 K under ultra-high vacuum (UHV) conditions [1]. Density functional theory (DFT) studies have confirmed that methane molecularly adsorbs on the IrO_2(110) surface and then cleaves its C–H bond with an activation barrier lower than 30 kJ mol^{-1} [13–15]. Despite the facile activation of methane on IrO_2(110), the superior reactivity of this catalyst also facilitates overoxidation to CO_x, hindering the selectivity towards value-added products. Other metal oxides such as RuO_2, RhO_2, and PdO are currently being investigated in the literature to find a catalyst with a moderate reactivity to improve selectivity [2,16,17]. Solar energy at room temperature can also be used for methane conversion and coupling via the photocatalytic oxidation route, which provides a low-energy and environmentally friendly alternative to thermocatalytic oxidation [18–20]. However, increasing the selectivity and yield of target value-added products by limiting the production of by-product CO_2 is crucial during photocatalytic oxidation and conversion of methane.

Non-oxidative coupling also provides an alternative route to circumvent the inevitable overoxidation to more thermodynamically stable products (CO_x) and produce C_2 products via:

$$2CH_4 \rightarrow C_2H_6 + H_2 \quad (3)$$

The initial C–H bond cleavage, however, remains the rate-limiting step in most catalytic materials previously examined. Conquering the high activation barrier of this step requires high temperatures, which accelerate coke deposition and catalyst deactivation, thus limiting the selectivity towards C_2 products. Some of the C_2 products formed, such as C_2H_6 and C_2H_4, may also further react to produce aromatics such as benzene instead of their desorption as final products, depending on the choice of catalyst.

Recently, transition metal phosphides (TMPs) have been explored for many different reactions, including selective C–S, C–N, and C–O activation, as well as methanol steam reforming, because of their unique selectivity and resistance to coking [21–25]. Dehydrogenative conversion of methane to higher hydrocarbons has also been investigated over silica-supported nickel phosphide catalysts [26,27]. These experimental results showed that the addition of phosphorus atoms to Ni increased the selectivity to higher hydrocarbons relative to coke from 3% to near 70% at temperatures of 1073–1148 K. This indicates that the reactivity of Ni could be controlled by the addition of P atoms, which may alter the electronic nature and geometry of the Ni surface. The mechanism of methane activation and conversion into higher hydrocarbons on nickel phosphide catalysts remains unclear.

Here, density functional theory (DFT) calculations were employed to examine non-oxidative methane activation and coupling pathways over Ni_2P catalyst. We show that methane activation occurs with a barrier of 246 kJ mol^{-1} on Ni_2P(001) surface. The addition of phosphorus atoms hinders the formation of deeply dehydrogenated species and promotes the selectivity towards CH_3* and CH_2* and their coupling reactions to produce C_2 products.

2. Results and Discussion

2.1. Optimized Structures and Binding Energies on Ni_2P(001) Surface

In this section, we examine the optimized structures and binding energies (ΔE_{ads}; Equation (4)) of CH_x* (x = 0–4) intermediates and H* on Ni_2P(001), as shown in Figure 1 and Table 1. The most stable adsorption mode for each species was determined after examining different adsorption sites on the Ni_2P(001) surface. CH_4* is weakly physisorbed, and it

does not directly interact with the $Ni_2P(001)$ surface (Figure 1a) because of its saturated coordination. In contrast, methane has been found to form a strong dative bond with the $IrO_2(110)$ surface, which weakens its C–H bonds and promotes C–H bond activation [1]. We have attempted initial configurations in which methane is directly interacting with either a surface Ni atom or a surface P atom through the carbon atom, but it eventually desorbed from the surface upon geometric convergence. It is worth noting that the RPBE functional used here neglects attractive dispersive forces that increase the binding energy of physisorbed species. For example, accounting for dispersion interactions using the RPBE-D3BJ method [28] increases the binding energy of CH_4* from −1 to −12 kJ mol^{-1}. However, these vdW-based methods often overestimate the binding energy of chemisorbed species by more than 50 kJ mol^{-1}. The inclusion of dispersive forces here would only shift the binding energy of chemisorbed species of similar size in approximately the same magnitude, thus relative barriers between elementary steps examined here would not be altered significantly.

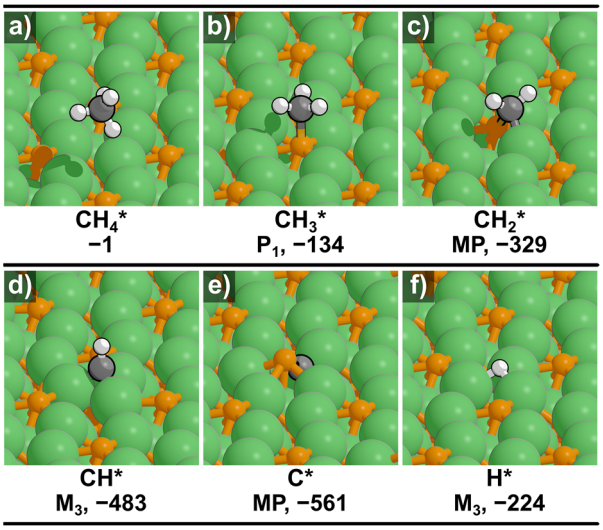

Figure 1. DFT-optimized structures for (**a**–**e**) CH_x* (x = 0–4) and (**f**) H*. The binding energies (in kJ mol^{-1}) and adsorption modes are shown beneath each image (see Section 3 for more details).

Table 1. DFT-predicted adsorbates binding energies ΔE_{ads} (Equation (4); kJ mol^{-1}) and adsorption modes on $Ni_2P(001)$. Average bond distances of the carbon atom with surface atoms are shown in Å.

Species	Adsorption Mode	ΔE_{ads} kJ mol^{-1}	d(C–Ni) (Å)	d(C–P) (Å)
CH_4*	Physisorbed	−1	–	–
CH_3*	P_1	−134	–	1.90
CH_2*	MP	−329	2.06	1.78
CH*	M_3	−483	1.89	–
C*	MP	−561	1.92	1.77
H*	M_3	−224	1.80	–

$CH_{0–3}$* species, on the other hand, chemically bond with the surface with binding energies that increase with decreasing the number of H atoms (Table 1). CH_3* favorably adsorbs on top of the P atom (P_1 site; Figure 1b) with a binding energy of −134 kJ mol^{-1} and a C–P bond distance of 1.90 Å. It can also adsorb on top of the Ni atom (M_1) or on a bridging site between two Ni atoms (M_2), but these adsorption modes are less favorable by 20 kJ mol^{-1}. CH_2* can either bind to the Ni–Ni (M_2) or Ni–P (MP) bridging sites, but the MP site (Figure 1c) is much more favorable with a binding energy of −329 kJ mol^{-1}, 43 kJ mol^{-1} more stable than that of the M_2 site. CH* binds more strongly to the 3-fold metal site (M_3; Figure 1d) with a binding energy of −483 kJ mol^{-1}, and C* has the strongest

binding energy among all CH_x species with a binding energy of −561 kJ mol^{-1}. Notably, the C* atom disrupts the $Ni_2P(001)$ surface by breaking the Ni–P bond and interacts with the subsurface atoms (Figure 1e). Lastly, the H* atom has a binding energy of −224 kJ mol^{-1}, and it preferably adsorbs on the M_3 site (Figure 1f). These findings indicate that more saturated species (e.g., CH_3* and CH_2*) generally exhibit a preference towards interacting with the P atoms instead of Ni atoms.

2.2. Methane Dehydrogenation Reactions

Here, we explore the dehydrogenation reactions of methane on the $Ni_2P(001)$ surface. Table 2 lists the forward activation barriers and reaction energies of the four successive dehydrogenation reactions of CH_4. These ΔH_{act} and ΔH_{rxn} values represent the differences between a transition state and the reactants, or the products and the reactants in their most stable adsorption sites. Different surface sites have been examined for each reaction to find the most stable transition state. The dehydrogenated H atoms are desorbed from the surface as $\frac{1}{2}H_{2(g)}$. Figure 2 displays the structures of the reactants, transition state, and products for each reaction. These reactants and products shown in this figure refer to the immediate initial and final states before and after the transition state, which do not include diffusion steps to more stable binding configurations.

Table 2. DFT-predicted forward activation enthalpy ($\Delta H_{act} = H_{TS} - H_{reactants}$) and enthalpy of reaction ($\Delta H_{rxn} = H_{products} - H_{reactants}$) for methane dehydrogenation reactions on $Ni_2P(001)$ at 1123 K.

No.	Reaction	ΔH_{act} kJ mol^{-1}	ΔH_{rxn} kJ mol^{-1}
1	$CH_4^* \rightarrow CH_3^* + \frac{1}{2}H_{2(g)}$	246	99
2	$CH_3^* \rightarrow CH_2^* + \frac{1}{2}H_{2(g)}$	65	44
3	$CH_2^* \rightarrow CH^* + \frac{1}{2}H_{2(g)}$	84	74
4	$CH^* \rightarrow C^* + \frac{1}{2}H_{2(g)}$	102	41

Physisorbed CH_4 reacts with a surface P atom and undergoes C−H bond activation with an adjacent Ni atom to form CH_3* on P_1 site and H* on M_3 site (Figure 2a). This reaction has an enthalpic barrier of 246 kJ mol^{-1} and is endothermic with a reaction energy of 99 kJ mol^{-1} (Table 2). This barrier is much larger than those reported previously on pure Ni [29], metal carbides [3,6], and metal oxides [1,2,30], indicating that $Ni_2P(001)$ surface is less reactive. Subsequent C–H bond activations have much lower activation barriers and reaction energies. Adsorbed CH_3* can undergo C−H bond cleavage with an activation barrier of 65 kJ mol^{-1} and a reaction energy of 44 kJ mol^{-1}. This reaction starts with CH_3* adsorbed on a P_1 site and proceeds to cleave the C–H bond with a vicinal Ni atom to form the CH_2* intermediate on a Ni–P bridging site and H* on the M_3 site (Figure 2b). The C–H bond activation of CH_2* to form CH* then requires an activation barrier of 84 kJ mol^{-1}, which is 19 kJ mol^{-1} higher than that of CH_2* formation from CH_3*. In this reaction, phosphorus atoms do not directly participate in binding the transition state or adsorbed species (Figure 3c). The last dehydrogenation reaction requires an activation barrier of 102 kJ mol^{-1} to form atomic carbon C* and an adjacent H* on M_3 sites (Figure 3d). Here, we do not observe the surface disruption caused by C* when it binds to the Ni–P bridging site. These trends in activation barriers of methane dehydrogenation are consistent with the reported trends on pure Ni surface in which the first and last dehydrogenation steps require higher activation barriers relative to CH_3* and CH_2* dehydrogenation [29]. However, the formation of CH* on Ni(111) is much more facile than CH_2* formation (by >35 kJ mol^{-1}), and CH* is likely the most abundant surface intermediate on Ni(111).

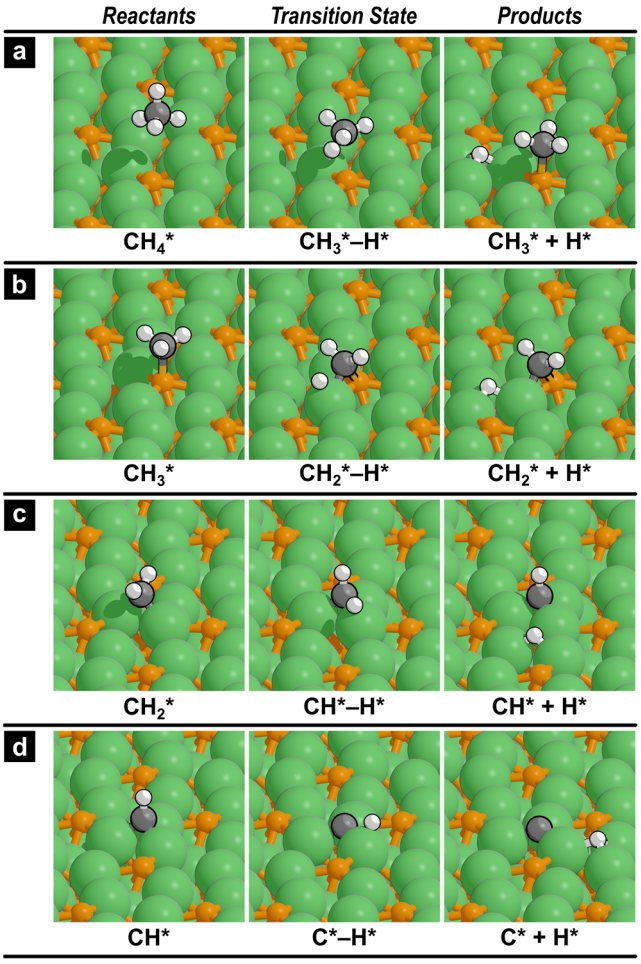

Figure 2. Reactants, transition state, and product structures for the dehydrogenation reaction of (**a**) CH_4, (**b**) CH_3, (**c**) CH_2, and (**d**) CH on $Ni_2P(001)$ surface.

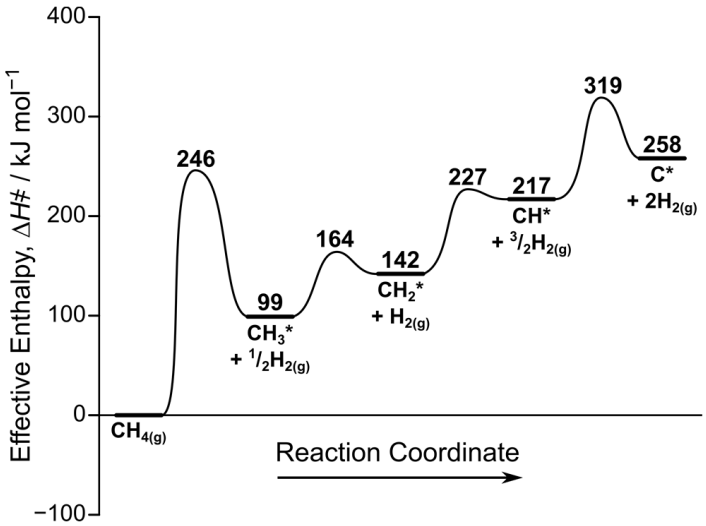

Figure 3. DFT-predicted reaction coordinate diagram for methane dehydrogenation on $Ni_2P(001)$ surface constructed using Equation (5) at 1123 K. Each CH_x species is adsorbed in its preferred adsorption site as discussed in Section 2.1.

Figure 3 shows the effective enthalpy (ΔH) reaction coordinate diagram calculated using Equation (5) relative to $CH_{4(g)}$ and a stoichiometric amount of $H_{2(g)}$. After the initial

C–H bond cleavage, the effective enthalpy barrier increases with each dehydrogenation step from 164 kJ mol^{-1} for CH_2* formation and 227 kJ mol^{-1} for CH* formation to 319 kJ mol^{-1} for the last dehydrogenation step to form C*. The C–H bond activation of CH* has the highest effective barrier among all four dehydrogenation steps, suggesting that carbon deposition on Ni_2P(001) is kinetically unfavorable. In contrast to Ni(111) surface, the formation of CH* requires a high effective barrier of 227 kJ mol^{-1}, and the backward barrier to form CH_2* is only 10 kJ mol^{-1}, indicating that either CH_2* or CH_3* is more likely to be the most abundant surface intermediate on Ni_2P. Therefore, selective dehydrogenation to CH_2* on Ni_2P(001) can be achieved by controlling the reaction conditions to prevent further dehydrogenation steps to CH* and C*, opening catalytic routes to produce ethane and ethylene via coupling reactions.

2.3. C–C Coupling Reactions

Next, we examine C_2 products formation from CH_x* intermediates via C–C coupling reactions on Ni_2P(001) surface. Table 3 lists the forward activation barriers and reaction energies for the C–C coupling reactions to form ethane (C_2H_6), ethylene (C_2H_4), and acetylene (C_2H_2). Values shown in this table are referenced to the reactants adsorbed separately in their most stable adsorption sites discussed in Section 2.1. CH_x* intermediates may diffuse from their most stable sites to a less stable site before the reaction occurs, but these diffusion steps are assumed to be fast. Figure 4 displays the structures of the reactants (immediately before the transition state), transition state, and products for each reaction. A CH_3* adsorbed on a P_1 site can react with another nearby CH_3* on a Ni–Ni bridging site to form ethane (Figure 4a) with an activation barrier of 98 kJ mol^{-1} and a reaction energy of −96 kJ mol^{-1} (relative to 2CH_3* both adsorbed on separate P_1 sites). The CH_3*–CH_3* coupling transition state occurs on a single Ni atom elevated away from the surface. The CH_2*–CH_2* coupling reaction occurs with a much lower activation barrier of 56 kJ mol^{-1} to form ethylene chemisorbed on a single Ni atom (Figure 4b). The desorption of ethylene from the surface requires only 7 kJ mol^{-1}. Similarly, the formation of acetylene from CH*–CH* coupling is also facile with an activation barrier of 56 kJ mol^{-1} (Figure 4c), but its desorption from the surface requires an energy of 100 kJ mol^{-1}. Given that CH_3* and CH_2* are expected to dominate the Ni_2P(001) surface instead of CH* and C* as discussed in the previous section, we can rule out the formation of acetylene on Ni_2P. We have also examined the possibility of coupling CH_3* and CH_2* to form *CH_3CH_2*, but this reaction requires a large activation barrier of 191 kJ mol^{-1} (Table 3); this is the highest activation barrier among all C–C coupling reactions examined here.

Table 3. DFT-predicted forward activation enthalpy ($\Delta H_{act} = H_{TS} - H_{reactants}$) and enthalpy of reaction ($\Delta H_{rxn} = H_{products} - H_{reactants}$) for the C–C coupling reactions on Ni_2P(001) at 1123 K.

No.	Reaction	ΔH_{act} kJ mol^{-1}	ΔH_{rxn} kJ mol^{-1}
1	CH_3* + CH_3*→*CH_3CH_3*	98	−96
2	CH_2* + CH_2*→*CH_2CH_2*	56	−79
3	CH* + CH*→*CHCH*	56	−133
4	CH_3* + CH_2*→*CH_3CH_2*	191	−31

These results are consistent with the experimental findings for SiO_2-supported nickel phosphide catalysts, which show a selectivity of near 70% towards ethane and ethylene formation from methane at 1123 K and negligible formation of acetylene [26,27]. Based on these results, we conclude that CH_3* may preferably undergo C–H bond activation with a forward activation barrier of 65 kJ mol^{-1} (Figure 3). Then, two CH_2* fragments can be coupled to form ethylene with a barrier of 56 kJ mol^{-1} (Table 3).

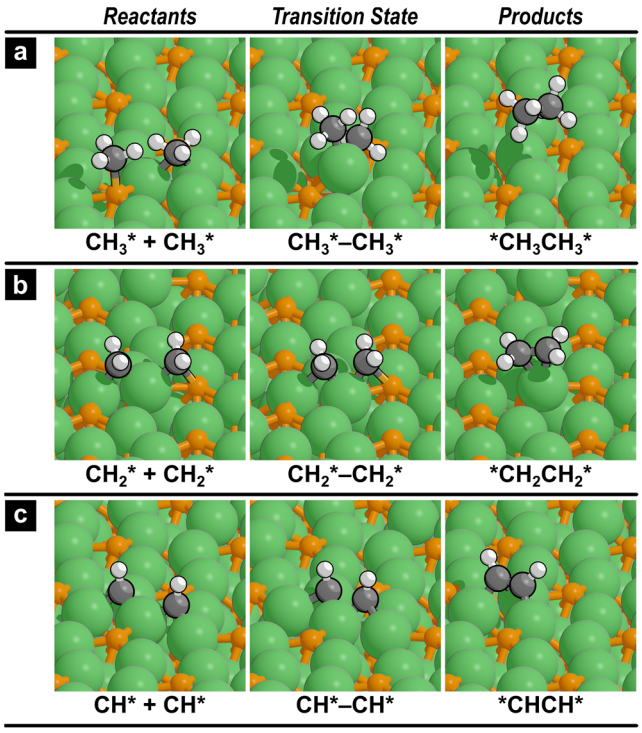

Figure 4. Reactants, transition state, and product structures for the C–C coupling reactions to form (**a**) CH_3CH_3, (**b**) CH_2CH_2, and (**c**) CHCH on $Ni_2P(001)$ surface.

3. Computational Methods

For the computational methods, the Vienna ab initio simulation package (VASP) was used to perform periodic density functional theory (DFT) calculations [31–34], and these calculations were implemented using the computational catalysis interface (CCI) [35]. Plane waves were constructed using projector augmented-wave (PAW) potentials [36,37] with an energy cutoff of 396 eV. The generalized gradient approximation (GGA) using the revised Perdew−Burke−Ernzerhof (RPBE) form was utilized to describe exchange and correlation energies [38–40]. A 11 × 11 × 11 Å unit cells of empty space were used to model gas-phase molecules. The unit cell of bulk Ni_2P was obtain from crystallographic data [41], and then the lattice parameters were optimized using DFT as detailed in our previous work [24]. DFT-predicted bulk lattice parameters (a = b = 5.87 Å and c = 3.37 Å) were in agreement with prior DFT and experimental studies (a = b = 5.86 Å and c = 3.38 Å) [42,43]. The DFT-simulated XRD patterns of bulk Ni_2P are shown in Figure S1 (Supplementary Materials). The Ni_2P surface does not exhibit ferromagnetic properties, as confirmed in previous studies [24,42], and thus, spin-polarized calculations were not used.

In our previous study [24], we examined the surface formation energy of different Ni_2P facets and showed that the Ni-rich termination of the $Ni_2P(001)$ surface exhibits the lowest surface formation energy (Figure S2; Supplementary Materials). Thus, the Ni-rich termination (Figure 5a) was used here to model the 2 × 2 $Ni_2P(001)$ surface, although other surfaces may also contribute, albeit to a lesser extent, to the measured rate. Four atomic layers (two repeating units) were built in the z-direction, and a vacuum region of 10 Å was added perpendicular to the surface (Figure 5b). The bottom half of the slab (two atomic layers) was fixed in its bulk position. A k-point mesh of 3 × 3 × 1 was used [44,45], and all systems were relaxed until the maximum force on each atom was <0.05 eVÅ^{-1}, while wave functions were converged to within 10^{-6} eV. The nudged elastic band (NEB) method and the dimer method were utilized to find transition-state structures [46–48]. Similar convergence criteria were used in the dimer method. In the NEB method, wave functions were converged to within 10^{-4} eV, and forces were converged to <0.5 eV Å^{-1}. Vibrational

frequency calculations were performed to estimate enthalpies for each state at 1123 K. The adsorbates binding energy (ΔE_{ads}) relative to the gas-phase species is defined as:

$$\Delta E_{ads} = E_{species/surf} - E_{species(g)} - E_{surf} \quad (4)$$

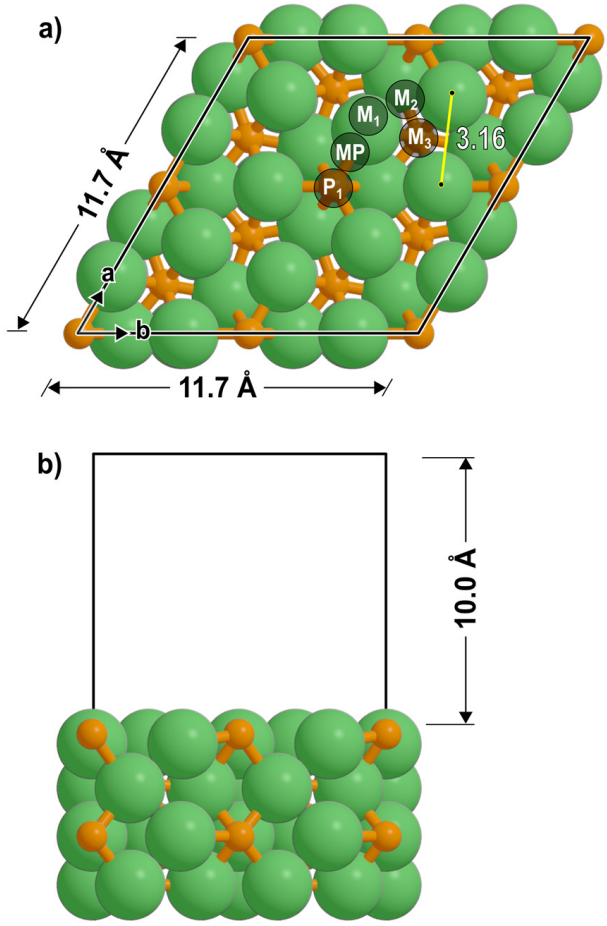

Figure 5. The $Ni_2P(001)$ model used in this study as shown from the (**a**) top and (**b**) side. The adsorption sites are labeled as follows M_1: metal atop, M_2: metal bridge, M_3: metal three-fold hollow, MP: metal-phosphorus bridge, and P_1: phosphorus atop. The bottom two atomic layers were fixed in their bulk positions during relaxation.

Thus, more negative values indicate stronger binding. Effective enthalpy barriers ($\Delta H^{\ddagger}$) are defined as the enthalpy of forming the transition state and a stoichiometric amount of gas-phase H_2 from gas-phase methane:

$$\Delta H^{\ddagger} = H^{\ddagger} + \lambda H_{H2(g)} - H_{CH4(g)} - H_{surf} \quad (5)$$

where λ is the number of H_2 molecules desorbed from the surface as a result of the dehydrogenation steps. Further details of the computational methods are reported in the Supplementary Materials (Section S1). Transition-state structures and reaction mode files, as well as adsorbate structure files, are also reported in the Supplementary Materials (Structures.zip).

4. Conclusions

Methane activation and coupling pathways on the $Ni_2P(001)$ surface were investigated using DFT. The incorporation of P atoms in Ni_2P decreases the reactivity of the catalytic surface but increases the selectivity towards value-added products. DFT-predicted barriers demonstrate that carbon deposition is kinetically unfavorable on Ni_2P, and that

CH_3* and CH_2* may dominate the catalytic surface after the initial C–H bond cleavage in methane. This is in stark contrast to pure Ni surface, where CH* was found to be the most abundant surface intermediate. Ethylene can be selectively produced on Ni_2P through $CH_4 \rightarrow CH_3^* \rightarrow CH_2^* \rightarrow 2CH_2^* \rightarrow C_2H_4$ by controlling the reaction conditions to block further dehydrogenation steps. The superior selectivity towards C_2 products and resistance to coke formation of Ni_2P make it an attractive catalyst for direct methane conversion to ethylene.

Supplementary Materials: The following supporting information can be downloaded at: https://www.mdpi.com/article/10.3390/catal13030531/s1, Section S1: Details of density functional calculations of thermochemical properties; Figure S1: Experimental and DFT-simulated XRD patterns of bulk Ni_2P; Figure S2: DFT-derived surface formation energy for Ni_2P. Structures.zip: transition-state structures and reaction mode files, as well as adsorbates structure files.

Author Contributions: Conceptualization, A.A. and Z.A.; methodology, A.A.; software, S.N.A., A.A.M., A.K.A. and M.A.A.; validation, A.A. and S.S.H.; formal analysis, A.A., S.N.A., A.A.M., A.K.A. and M.A.A.; investigation, A.A., S.N.A., A.A.M., A.K.A. and M.A.A.; resources, A.A.; data curation, A.A. and S.S.H.; writing—original draft preparation, A.A.; writing—review and editing, A.A., Z.A. and S.S.H.; visualization, A.A. and Z.A.; supervision, A.A.; project administration, A.A.; funding acquisition, A.A. All authors have read and agreed to the published version of the manuscript.

Funding: The authors extend their appreciation to the Deputyship for Research & Innovation, Ministry of Education in Saudi Arabia for funding this research work through project number: [INST141].

Data Availability Statement: Not applicable.

Conflicts of Interest: The authors declare no conflict of interest.

References

1. Liang, Z.; Li, T.; Kim, M.; Asthagiri, A.; Weaver, J.F. Low-Temperature Activation of Methane on the IrO_2(110) Surface. *Science* **2017**, *356*, 299–303. [CrossRef]
2. Kim, D.; Ju, Y.; Kang, D.; Kang, S.B.; Kim, M. Potential of Intrinsic Reactivity toward Value Added Products from Methane Oxidation on RhO_2(1 1 0) Surface. *Appl. Surf. Sci.* **2022**, *596*, 153499. [CrossRef]
3. Zhang, T.; Holiharimanana, D.; Yang, X.; Ge, Q. DFT Study of Methane Activation and Coupling on the (0001) and (112¯ 0) Surfaces of α-WC. *J. Phys. Chem. C* **2020**, *124*, 26722–26729. [CrossRef]
4. Boekfa, B.; Treesukol, P.; Injongkol, Y.; Maihom, T.; Maitarad, P.; Limtrakul, J. The Activation of Methane on Ru, Rh, and Pd Decorated Carbon Nanotube and Boron Nitride Nanotube: A DFT Study. *Catalysts* **2018**, *8*, 190. [CrossRef]
5. Sun, X.; Li, X.; Liu, Y.; Yu, Z.; Li, B.; Zhao, Z. The C-H Bond Activation Triggered by Subsurface Mo Dopant on MgO Catalyst in Oxidative Coupling of Methane. *Catalysts* **2022**, *12*, 1083. [CrossRef]
6. Zhang, T.; Yang, X.; Ge, Q. A DFT Study of Methane Conversion on Mo-Terminated Mo2C Carbides: Carburization vs C–C Coupling. *Catal. Today* **2021**, *368*, 140–147. [CrossRef]
7. Rosen, A.S.; Notestein, J.M.; Snurr, R.Q. Structure-Activity Relationships That Identify Metal-Organic Framework Catalysts for Methane Activation. *ACS Catal.* **2019**, *9*, 3576–3587. [CrossRef]
8. Mehmood, A.; Chae, S.Y.; Park, E.D. Photoelectrochemical Conversion of Methane into Value-Added Products. *Catalysts* **2021**, *11*, 1387. [CrossRef]
9. Latimer, A.A.; Kakekhani, A.; Kulkarni, A.R.; Nørskov, J.K. Direct Methane to Methanol: The Selectivity–Conversion Limit and Design Strategies. *ACS Catal.* **2018**, *8*, 6894–6907. [CrossRef]
10. West, N.M.; Miller, A.J.M.; Labinger, J.A.; Bercaw, J.E. Homogeneous Syngas Conversion. *Coord. Chem. Rev.* **2011**, *255*, 881–898. [CrossRef]
11. Blanksby, S.J.; Ellison, G.B. Bond Dissociation Energies of Organic Molecules. *Acc Chem. Res.* **2003**, *36*, 255–263. [CrossRef] [PubMed]
12. Keller, G. Synthesis of Ethylene via Oxidative Coupling of Methane I. Determination of Active Catalysts. *J. Catal.* **1982**, *73*, 9–19. [CrossRef]
13. Kim, M.; Franklin, A.; Martin, R.; Feng, F.; Li, T.; Liang, Z.; Asthagiri, A.; Weaver, J.F. Adsorption and Oxidation of CH_4 on Oxygen-Rich IrO_2 (110). *J. Phys. Chem. C* **2019**, *123*, 27603–27614. [CrossRef]
14. Kim, M.; Franklin, A.D.; Martin, R.; Bian, Y.; Weaver, J.F.; Asthagiri, A. Kinetics of Low-Temperature Methane Activation on IrO_2(1 1 0): Role of Local Surface Hydroxide Species. *J. Catal.* **2020**, *383*, 181–192. [CrossRef]

15. Wang, C.-C.; Siao, S.S.; Jiang, J.-C. C–H Bond Activation of Methane via σ–d Interaction on the IrO_2(110) Surface: Density Functional Theory Study. *J. Phys. Chem. C* **2012**, *116*, 6367–6370. [CrossRef]
16. Erlekam, U.; Paulus, U.A.; Wang, Y.; Bonzel, H.P.; Jacobi, K.; Ertl, G. Adsorption of Methane and Ethane on RuO_2(110) Surfaces. *Z. Für Phys. Chem.* **2005**, *219*, 891–903. [CrossRef]
17. Weaver, J.F.; Hakanoglu, C.; Hawkins, J.M.; Asthagiri, A. Molecular Adsorption of Small Alkanes on a PdO(101) Thin Film: Evidence of σ-Complex Formation. *J. Chem. Phys.* **2010**, *132*, 024709. [CrossRef] [PubMed]
18. Huang, A.; Wang, J.; Wu, X.; Liu, H.; Cai, J.; Xu, G.Q.; Wang, S.L. Room-Temperature Coupling of Methane with Singlet Oxygen. *Environ. Sci. Adv.* **2022**, *1*, 438–442. [CrossRef]
19. Wu, X.Y.; Tang, Z.; Zhao, X.; Luo, X.; John Pennycook, S.; Wang, S.L. Visible-Light Driven Room-Temperature Coupling of Methane to Ethane by Atomically Dispersed Au on WO3. *J. Energy Chem.* **2021**, *61*, 195–202. [CrossRef]
20. Zeng, Y.; Luo, X.; Li, F.; Huang, A.; Wu, H.; Xu, G.Q.; Wang, S.L. Noble Metal-Free FeOOH/$Li_{0.1}$ WO_3 Core–Shell Nanorods for Selective Oxidation of Methane to Methanol with Visible–NIR Light. *Environ. Sci. Technol.* **2021**, *55*, 7711–7720. [CrossRef]
21. Li, W.; Dhandapani, B.; Oyama, S.T. Molybdenum Phosphide: A Novel Catalyst for Hydrodenitrogenation. *Chem. Lett.* **1998**, *27*, 207–208. [CrossRef]
22. Bui, P.; Cecilia, J.A.; Oyama, S.T.; Takagaki, A.; Infantes-Molina, A.; Zhao, H.; Li, D.; Rodríguez-Castellón, E.; Jiménez López, A. Studies of the Synthesis of Transition Metal Phosphides and Their Activity in the Hydrodeoxygenation of a Biofuel Model Compound. *J. Catal.* **2012**, *294*, 184–198. [CrossRef]
23. Almithn, A.; Alhulaybi, Z. A Mechanistic Study of Methanol Steam Reforming on Ni2P Catalyst. *Catalysts* **2022**, *12*, 1174. [CrossRef]
24. Witzke, M.E.; Almithn, A.; Conrad, C.L.; Hibbitts, D.D.; Flaherty, D.W. Mechanisms and Active Sites for C–O Bond Rupture within 2-Methyltetrahydrofuran over Ni, $Ni_{12}P_5$, and Ni_2P Catalysts. *ACS Catal.* **2018**, *8*, 7141–7157. [CrossRef]
25. Witzke, M.E.; Almithn, A.; Conrad, C.L.; Triezenberg, M.D.; Hibbitts, D.D.; Flaherty, D.W. In Situ Methods for Identifying Reactive Surface Intermediates during Hydrogenolysis Reactions: C–O Bond Cleavage on Nanoparticles of Nickel and Nickel Phosphides. *J. Am. Chem. Soc.* **2019**, *141*, 16671–16684. [CrossRef]
26. Dipu, A.L.; Nishikawa, Y.; Inami, Y.; Iguchi, S.; Yamanaka, I. Development of Highly Active Silica-Supported Nickel Phosphide Catalysts for Direct Dehydrogenative Conversion of Methane to Higher Hydrocarbons. *Catal. Lett.* **2022**, *152*, 199–212. [CrossRef]
27. Dipu, A.L.; Ohbuchi, S.; Nishikawa, Y.; Iguchi, S.; Ogihara, H.; Yamanaka, I. Direct Nonoxidative Conversion of Methane to Higher Hydrocarbons over Silica-Supported Nickel Phosphide Catalyst. *ACS Catal.* **2020**, *10*, 375–379. [CrossRef]
28. Grimme, S.; Ehrlich, S.; Goerigk, L. Effect of the Damping Function in Dispersion Corrected Density Functional Theory. *J. Comput. Chem.* **2011**, *32*, 1456–1465. [CrossRef]
29. Han, Z.; Yang, Z.; Han, M. Comprehensive Investigation of Methane Conversion over Ni(111) Surface under a Consistent DFT Framework: Implications for Anti-Coking of SOFC Anodes. *Appl. Surf. Sci.* **2019**, *480*, 243–255. [CrossRef]
30. Pham, T.L.M.; Leggesse, E.G.; Jiang, J.C. Ethylene Formation by Methane Dehydrogenation and C-C Coupling Reaction on a Stoichiometric IrO_2(110) Surface—A Density Functional Theory Investigation. *Catal. Sci. Technol.* **2015**, *5*, 4064–4071. [CrossRef]
31. Kresse, G.; Hafner, J. *Ab Initio* Molecular Dynamics for Liquid Metals. *Phys. Rev. B* **1993**, *47*, 558–561. [CrossRef]
32. Kresse, G.; Hafner, J. *Ab Initio* Molecular-Dynamics Simulation of the Liquid-Metal–Amorphous-Semiconductor Transition in Germanium. *Phys. Rev. B* **1994**, *49*, 14251–14269. [CrossRef] [PubMed]
33. Kresse, G.; Furthmüller, J. Efficient Iterative Schemes for *Ab Initio* Total-Energy Calculations Using a Plane-Wave Basis Set. *Phys. Rev. B* **1996**, *54*, 11169–11186. [CrossRef] [PubMed]
34. Kresse, G.; Furthmüller, J. Efficiency of Ab-Initio Total Energy Calculations for Metals and Semiconductors Using a Plane-Wave Basis Set. *Comput. Mater. Sci.* **1996**, *6*, 15–50. [CrossRef]
35. Kravchenko, P.; Plaisance, C.; Hibbitts, D. A New Computational Interface for Catalysis. *ChemRxiv* **2019**, preprint.
36. Blöchl, P.E. Projector Augmented-Wave Method. *Phys. Rev. B* **1994**, *50*, 17953–17979. [CrossRef]
37. Kresse, G.; Joubert, D. From Ultrasoft Pseudopotentials to the Projector Augmented-Wave Method. *Phys. Rev. B* **1999**, *59*, 1758–1775. [CrossRef]
38. Hammer, B.; Hansen, L.B.; Nørskov, J.K. Improved Adsorption Energetics within Density-Functional Theory Using Revised Perdew-Burke-Ernzerhof Functionals. *Phys. Rev. B* **1999**, *59*, 7413–7421. [CrossRef]
39. Perdew, J.P.; Burke, K.; Ernzerhof, M. Generalized Gradient Approximation Made Simple. *Phys. Rev. Lett.* **1996**, *77*, 3865–3868. [CrossRef]
40. Zhang, Y.; Yang, W. Comment on "Generalized Gradient Approximation Made Simple". *Phys. Rev. Lett.* **1998**, *80*, 890. [CrossRef]
41. Larsson, E. An X-Ray Investigation of Ni-P System and Crystal Structures of NiP and NiP2. *Arkiv. Kemi.* **1965**, *23*, 335.
42. Rem, J.; Wang, J.; Li, J.; Li, Y. Density Functional Theory Study on Crystal Nickel Phosphides. *J. Fuel Chem. Technol.* **2007**, *35*, 458–464. [CrossRef]
43. Rundqvist, S. X-Ray Investigations of Mn3P, Mn2P, and Ni2P. *Acta Chem. Scand* **1962**, *16*, 992–998. [CrossRef]
44. Monkhorst, H.J.; Pack, J.D. Special Points for Brillouin-Zone Integrations. *Phys. Rev. B* **1976**, *13*, 5188–5192. [CrossRef]
45. Pack, J.D.; Monkhorst, H.J. "Special Points for Brillouin-Zone Integrations"—A Reply. *Phys. Rev. B* **1977**, *16*, 1748–1749. [CrossRef]
46. Henkelman, G.; Jónsson, H. Improved Tangent Estimate in the Nudged Elastic Band Method for Finding Minimum Energy Paths and Saddle Points. *J. Chem. Phys.* **2000**, *113*, 9978–9985. [CrossRef]

47. Jónsson, H.; Mills, G.; Jacobsen, K.W. Nudged Elastic Band Method for Finding Minimum Energy Paths of Transitions. In Proceedings of the Classical and Quantum Dynamics in Condensed Phase Simulations, Lerici, Italy, 7—18 July 1997; World Scientific: Singapore, 1998; pp. 385–404.
48. Henkelman, G.; Jónsson, H. A Dimer Method for Finding Saddle Points on High Dimensional Potential Surfaces Using Only First Derivatives. *J. Chem. Phys.* **1999**, *111*, 7010–7022. [CrossRef]